Using infinite-volume, continuum QED and lattice QCD for the hadronic light-by-light contribution to the muon anomalous magnetic moment

Thomas Blum,[1,2] Norman Christ,[3] Masashi Hayakawa,[4] Taku Izubuchi,[5,2]
Luchang Jin,[5,*] Chulwoo Jung,[5] and Christoph Lehner[5]

[1]*Physics Department, University of Connecticut, Storrs, Connecticut 06269-3046, USA*
[2]*RIKEN BNL Research Center, Brookhaven National Laboratory, Upton, New York 11973, USA*
[3]*Physics Department, Columbia University, New York, New York 10027, USA*
[4]*Department of Physics, Nagoya University, Nagoya 464-8602, Japan*
[5]*Physics Department, Brookhaven National Laboratory, Upton, New York 11973, USA*

In our previous work, Blum *et al.* [Phys. Rev. Lett. **118**, 022005 (2017)], the connected and leading disconnected hadronic light-by-light contributions to the muon anomalous magnetic moment $(g - 2)$ have been computed using lattice QCD ensembles corresponding to physical pion mass generated by the RBC/UKQCD Collaboration. However, the calculation is expected to suffer from a significant finite-volume error that scales like $1/L^2$ where L is the spatial size of the lattice. In this paper, we demonstrate that this problem is cured by treating the muon and photons in infinite-volume, continuum QED, resulting in a weighting function that is precomputed and saved with affordable cost and sufficient accuracy. We present numerical results for the case when the quark loop is replaced by a muon loop, finding the expected exponential approach to the infinite volume limit and consistency with the known analytic result. We have implemented an improved weighting function which reduces both discretization and finite-volume effects arising from the hadronic part of the amplitude.

I. INTRODUCTION

Precision measurements of lepton magnetic dipole moments provide a powerful tool for testing the standard model (SM) of particle physics at high precision. The magnetic dipole moment $\vec{\mu}$ originating from the lepton's spin $\vec{s}$ is commonly expressed as

$$\vec{\mu} = g \left(\frac{e}{2m} \right) \vec{s}, \qquad (1)$$

where e is the lepton's electromagnetic charge and m is its mass. The anomalous magnetic moment, or anomaly, $a = (g - 2)/2$ expresses the deviation from Dirac's relativistic quantum-mechanical prediction $g = 2$. It is generated by small radiative corrections, which, by a careful comparison between its experimental measurement to its theory prediction, may reveal physics beyond the standard model. Experimental measurements have determined these anomalous moments at very high precision. The electron anomaly, $a_e = 0.00115965218073(28)$ [1], currently yields the most precise value of the fine structure constant $\alpha = 1/137.035999157(33)$ [2]. In general, contributions from a new physics scale Λ_{NP} to the anomalous magnetic moment of a lepton $\ell = e, \mu, \tau$ are suppressed by $m_\ell^2/\Lambda_{\mathrm{NP}}^2$. One therefore expects the muon to be 5 orders of magnitude more sensitive to such contributions than the electron

which outweighs a loss in experimental precision. With the τ being experimentally inaccessible, a_μ is the most promising channel to reveal physics beyond the standard model.

Interestingly, current experimental and theoretical determinations of a_μ differ at the 3.1–3.5 standard deviation level,

$$
\begin{aligned}
a_\mu^{\mathrm{EXP}} - a_\mu^{\mathrm{SM}} &= (27.6 \pm 8.0) \times 10^{-10} \, [17], \\
&\quad (25.0 \pm 8.0) \times 10^{-10} \, [18], \qquad (2)
\end{aligned}
$$

depending on which value for the hadronic vacuum polarization contribution is used (see Table I).

In this tension the theory and experimental uncertainties are approximately balanced, with the theory uncertainty dominated by the hadronic vacuum polarization and hadronic light-by-light (HLbL) contributions. With future experiments at Fermilab (E989) [9] and J-PARC (E34) [10] aiming for a fourfold decrease in experimental uncertainty, a careful first-principles determination of these hadronic contributions and a similar reduction in uncertainty is desirable.

In this work we present an improved method of computing the HLbL contribution from first principles in lattice quantum chromodynamics (QCD). We build on the optimized sampling strategy of the HLbL diagrams, which we have introduced in Ref. [11], and which has reduced the statistical uncertainties, at the same cost, by more than an

---

*ljin.luchang@gmail.com

TABLE I. Individual contributions to the current standard model calculation of a_μ [3,4]. The BNL E821 experimental result [5] and Fermilab E989 target precision [6] are given for comparison.

Contribution	Value $\times 10^{10}$	Uncertainty $\times 10^{10}$
QED	11 658 471.895	0.008
Electroweak Corrections	15.4	0.1
HVP (LO) [7]	692.3	4.2
HVP (LO) [8]	694.9	4.3
HVP (NLO)	−9.84	0.06
HVP (NNLO)	1.24	0.01
HLbL	10.5	2.6
Total SM prediction [7]	11 659 181.5	4.9
Total SM prediction [8]	11 659 184.1	5.0
BNL E821 result	11 659 209.1	6.3
Fermilab E989 target		≈1.6

order of magnitude compared to the pioneering work of Ref. [12]. In a recent publication [13], we have presented a first-principles $2 + 1$ flavor lattice QCD calculation of the connected and leading disconnected contributions to the muon anomaly at physical quark and muon masses,

$$a_\mu^{\mathrm{HLbL}} = 5.35(1.35) \times 10^{-10}, \qquad (3)$$

where the statistical uncertainty is given. This result is affected by potentially large systematic errors due to the nonzero lattice spacing and the finite lattice volume used in

our calculation. We are in the process of repeating our calculation on a second lattice spacing to address the former systematic. The latter is addressed in this work.

So far, all lattice QCD calculations of the HLbL contribution to the muon $g - 2$ have treated the photons and muon in the same finite hypercubic lattice where the quarks and gluons live. The results are expected to suffer from sizable finite-volume corrections, which scale as some power of the system size rather than the exponential scaling observed for typical lattice QCD calculations since the photons are restricted to a finite box. Inspired by earlier work on the hadronic vacuum polarization [14], we remove power-law finite-volume errors by computing the muon and photon components of our diagrams in infinite-volume and subsequently combine the resulting weight function with a QCD four-point function obtained in our lattice simulation. The Mainz group announced a similar approach [15,16], which, to a large extent, motivated this work.

In the following we describe our method in detail and verify it in the leptonic case, where we replace the quark by a lepton loop. This replacement is trivial from the perspective of our lattice calculation, and the same setup with free propagators replaced by propagators on a nontrivial QCD background allows us to perform the calculation in the desired QCD case.

In Ref. [11], we introduced a formula to obtain the connected hadronic light-by-light contribution to the anomalous magnetic moment given by the electromagnetic Pauli form factor evaluated at zero momentum transfer, $F_2(q^2 = 0)$, from a lattice calculation:

$$\frac{F_2^{\mathrm{cHLbL}}(q^2 = 0)}{m} \frac{(\sigma_{s',s})_i}{2} = \frac{1}{VT} \sum_{x,y,z} \sum_{x_{\mathrm{op}}} \frac{1}{2} \epsilon_{i,j,k} (x_{\mathrm{op}} - x_{\mathrm{ref}})_j \cdot i\bar{u}_{s'}(\vec{0}) \mathcal{F}_k^C(x, y, z, x_{\mathrm{op}}) u_s(\vec{0}), \qquad (4)$$

where $(\sigma_{s',s})_i = \bar{u}_{s'}(\vec{0}) \Sigma_i u_s(\vec{0})$ are the conventional Pauli matrices. The coordinates x_{op}, x, y, and z are the locations of the electromagnetic currents on the quark loop, the former corresponding to the external photon and the latter to the virtual photons connecting the quark loop to the muon (see Fig. 1). The point x_{ref} can be chosen arbitrarily and may even depend on x, y, and z. In Ref. [11], we set $x_{\mathrm{ref}} = (x + y)/2$ and further manipulated the above formula to take advantage of the symmetry between x, y, and z to reduce the statistical noise inherent in our Monte Carlo integration:

$$\frac{F_2^{\mathrm{cHLbL}}(q^2 = 0)}{m} \frac{(\sigma_{s',s})_i}{2} = \sum_{r,\tilde{z}} \mathfrak{Z}\left(\frac{r}{2}, -\frac{r}{2}, \tilde{z}\right) \sum_{\tilde{x}_{\mathrm{op}}} \frac{1}{2} \epsilon_{i,j,k} (\tilde{x}_{\mathrm{op}})_j \cdot i\bar{u}_{s'}(\vec{0}) \mathcal{F}_k^C\left(\frac{r}{2}, -\frac{r}{2}, \tilde{z}, \tilde{x}_{\mathrm{op}}\right) u_s(\vec{0}). \qquad (5)$$

The integration variables are related to the coordinates in Fig. 1 by the following equations: $r = x - y$, $\tilde{z} = z - (x + y)/2$, and $\tilde{x}_{\mathrm{op}} = x_{\mathrm{op}} - (x + y)/2$. The function "$\mathfrak{Z}$" is defined by

$$\mathfrak{Z}(x, y, z) = \begin{cases} 3 & \text{if } |x - y| < |x - z| \quad \text{and} \quad |x - y| < |y - z| \\ 3/2 & \text{if } |x - y| = |x - z| < |y - z| \quad \text{or} \quad |x - y| = |y - z| < |x - z| \\ 1 & \text{if } |x - y| = |x - z| = |y - z| \\ 0 & \text{otherwise.} \end{cases} \qquad (6)$$
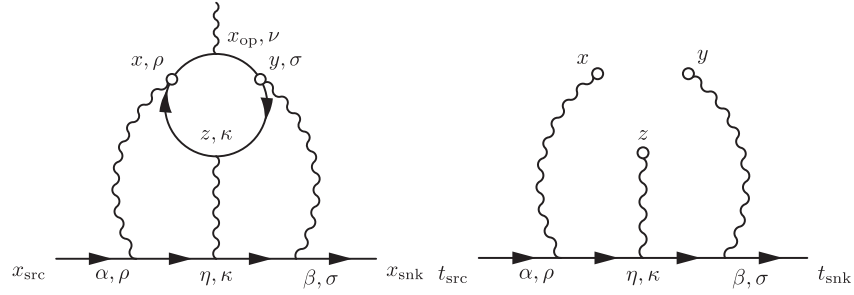
FIG. 1. The connected light-by-light diagram. There are five other diagrams like the one on the left that correspond to distinct ways of connecting the photons to the muon line (or, equivalently, the quark loop).

We compute the summation over r in Eq. (5) by stochastically sampling x and y point pairs, while the sums over $\tilde{x}_{\mathrm{op}}$ and $\tilde{z}$ are performed completely over the entire lattice. The amplitude $\mathcal{F}_\nu^C(x, y, z, x_{\mathrm{op}})$ is given by

$$\mathcal{F}_\nu^C(x, y, z, x_{\mathrm{op}}) = (-ie)^6 \mathcal{G}_{\rho,\sigma,\kappa}(x, y, z) \mathcal{H}_{\rho,\sigma,\kappa,\nu}^C(x, y, z, x_{\mathrm{op}}), \tag{7}$$

where $i^4 \mathcal{H}_{\rho,\sigma,\kappa,\nu}^C(x, y, z, x_{\mathrm{op}})$ represents the four-point hadronic correlation function, and $i^3 \mathcal{G}_{\rho,\sigma,\kappa}(x, y, z)$ is the QED weighting function. For the connected diagram, $i^4 \mathcal{H}_{\rho,\sigma,\kappa,\nu}^C(x, y, z, x_{\mathrm{op}})$ is given by the following two equations:

$$i^4 \mathcal{H}_{\rho,\sigma,\kappa,\nu}^C(x, y, z, x_{\mathrm{op}}) = \frac{1}{6}\mathcal{H}_{\rho,\sigma,\kappa,\nu}(x, y, z, x_{\mathrm{op}}) + \frac{1}{6}\mathcal{H}_{\sigma,\kappa,\rho,\nu}(y, z, x, x_{\mathrm{op}}) + \frac{1}{6}\mathcal{H}_{\kappa,\rho,\sigma,\nu}(z, x, y, x_{\mathrm{op}})$$
$$+ \frac{1}{6}\mathcal{H}_{\kappa,\sigma,\rho,\nu}(z, y, x, x_{\mathrm{op}}) + \frac{1}{6}\mathcal{H}_{\rho,\kappa,\sigma,\nu}(x, z, y, x_{\mathrm{op}}) + \frac{1}{6}\mathcal{H}_{\sigma,\rho,\kappa,\nu}(y, x, z, x_{\mathrm{op}}), \tag{8}$$

$$\mathcal{H}_{\rho,\sigma,\kappa,\nu}(x, y, z, x_{\mathrm{op}}) = \sum_{q=u,d,s} (e_q/e)^4 \langle -\mathrm{tr}[i\gamma_\rho S_q(x, z)i\gamma_\kappa S_q(z, y)i\gamma_\sigma S_q(y, x_{\mathrm{op}})i\gamma_\nu S_q(x_{\mathrm{op}}, x)]\rangle_{\mathrm{QCD}}, \tag{9}$$

where $e_u/e = 2/3$ and $e_d/e = e_s/e = -1/3$. The QED weighting function, $i^3 \mathcal{G}_{\rho,\sigma,\kappa}(x, y, z)$, is a symmetrized version of $\mathfrak{G}_{\sigma,\kappa,\rho}(y, z, x)$, which is represented by the right diagram of Fig. 1:

$$i^3 \mathcal{G}_{\rho,\sigma,\kappa}(x, y, z) = \mathfrak{G}_{\rho,\sigma,\kappa}(x, y, z) + \mathfrak{G}_{\sigma,\kappa,\rho}(y, z, x) + \mathfrak{G}_{\kappa,\rho,\sigma}(z, x, y)$$
$$+ \mathfrak{G}_{\kappa,\sigma,\rho}(z, y, x) + \mathfrak{G}_{\rho,\kappa,\sigma}(x, z, y) + \mathfrak{G}_{\sigma,\rho,\kappa}(y, x, z), \tag{10}$$

$$\mathfrak{G}_{\sigma,\kappa,\rho}(y, z, x) = \lim_{t_{\mathrm{src}} \to -\infty, t_{\mathrm{snk}} \to \infty} e^{m_\mu(t_{\mathrm{snk}} - t_{\mathrm{src}})} \int_{\alpha,\beta,\eta} G(x, \alpha)G(y, \beta)G(z, \eta)$$
$$\times \int_{\vec{x}_{\mathrm{snk}},\vec{x}_{\mathrm{src}}} S_\mu(x_{\mathrm{snk}}, \beta)i\gamma_\sigma S_\mu(\beta, \eta)i\gamma_\kappa S_\mu(\eta, \alpha)i\gamma_\rho S_\mu(\alpha, x_{\mathrm{src}}), \tag{11}$$

where S_μ and G are free muon and photon propagators, respectively.

In the past, we evaluated the QED weighting function, $i^3 \mathcal{G}_{\rho,\sigma,\kappa}(x, y, z)$, on a finite size lattice, which resulted in $1/L^2$ finite-volume errors, where L is the size of the lattice that is used to evaluate $i^3 \mathcal{G}_{\rho,\sigma,\kappa}(x, y, z)$ [11]. This lattice was referred to as the QED box. Although one can make the QED box much larger than the QCD box [17], it is far better to compute the QED weighting function in infinite volume (and in the continuum) directly as proposed in Refs. [15,16].

It may be useful to recall the finite-volume effects expected in the calculation of the hadronic light-by-light scattering contributions we are studying. The mass gap of QCD has two implications for a hadronic correlation function such as $\mathcal{H}_{\rho,\sigma,\kappa,\nu}^C(x, y, z, x_{\mathrm{op}})$: (1) The correlation function will decrease exponentially as the space-time distances between its arguments grow; (2) for fixed locations of its arguments, the finite-volume errors in such a correlation function will fall exponentially in the linear

size of the volume in which it is computed. Therefore, if we evaluate the QED weighting function in infinite-volume, which is the focus of this paper, and keep the positions $x; y; z; x_{op}$ fixed, all finite-volume errors will be exponentially suppressed as the linear lattice size grows. Since the QED weighting does not grow exponentially when the separations between x, y, z increase, the summation in Eq. (5) converges exponentially implying that all finite-volume errors in the result for the muon anomaly are exponentially suppressed. For the same reason, one concludes that the finite-volume errors for the lattice calculation of the hadronic vacuum polarization (HVP) contribution to the muon $g-2$ [14] decrease exponentially as the lattice volume is increased. This conclusion will remain true when the QED corrections are included, if they are treated by a method similar to that used here. One should keep in mind that the use of an infinite-volume photon propagator in other contexts may not achieve the same reduction of finite-volume errors in the HLbL case studied here.

In this work, we demonstrate our method of computing the QED weighting function in infinite-volume, which differs significantly from the one proposed in Ref. [15]. The paper is organized as follows: In Sec. II, we perform some analytic calculations and reduce the 12-dimensional integration in $\mathfrak{G}_{\sigma,\kappa,\rho}(y,z,x)$ to a four-dimensional integration, which we then integrate numerically with the CUBA library cubature rules [18]. We also introduce a subtraction for $\mathfrak{G}_{\sigma,\kappa,\rho}(y,z,x)$, which does not alter the final result for F_2 in the infinite-volume and continuum limits of the QCD part. In Sec. III, we show results of a pure QED light-by-light calculation carried out in a fashion similar to that of Ref. [11], but using the new infinite-volume QED weighting function, and we compare the two. In addition, we demonstrate that the new subtracted QED weighting

function reduces the remaining exponentially suppressed finite-volume and $\mathcal{O}(a^2)$ discretization errors for F_2.

II. FORMULATION

Here we show how $\mathfrak{G}_{\sigma,\kappa,\rho}(y,z,x)$ is evaluated using Eq. (11) in infinite-volume. As usual, we work in Euclidean space-time, and the free muon and photon propagator take the form

$$S_\mu(x,y) = \int \frac{d^4p}{(2\pi)^4} \frac{1}{i\not{p}+m} e^{ip\cdot(x-y)}$$
$$= (-\not{\partial}_x + m) \int \frac{d^4p}{(2\pi)^4} \frac{1}{p^2+m^2} e^{ip\cdot(x-y)}, \quad (12)$$

$$G(x,y) = \int \frac{d^4p}{(2\pi)^4} \frac{1}{p^2} e^{ip\cdot(x-y)} = \frac{1}{4\pi^2} \frac{1}{(x-y)^2}. \quad (13)$$

The wall-source and sink muon propagators that create and annihilate muons at rest appropriate for our kinematic setup can be evaluated as

$$\lim_{t_{snk}\to\infty} e^{m_\mu t_{snk}} \int_{\vec{x}_{snk}} S_\mu(x_{snk},\beta) = \frac{\gamma_0+1}{2} e^{m_\mu \beta_t}, \quad (14)$$

$$\lim_{t_{src}\to-\infty} e^{-m_\mu t_{src}} \int_{\vec{x}_{src}} S_\mu(\alpha,x_{src}) = \frac{\gamma_0+1}{2} e^{-m_\mu \alpha_t}. \quad (15)$$

The matrix $\frac{\gamma_0+1}{2}$ is a projection operator, so

$$\mathfrak{G}_{\sigma,\kappa,\rho}(y,z,x) = \frac{\gamma_0+1}{2} \mathfrak{G}_{\sigma,\kappa,\rho}(y,z,x) \frac{\gamma_0+1}{2}. \quad (16)$$

Since m_μ is the only relevant scale in this function, without loss of generality, we set $m_\mu = 1$. Starting with Eqs. (14) and (15), we find

$$\lim_{t_{snk}\to\infty} e^{m_\mu(t_{snk}-\eta_t)} \int_\beta G(y,\beta) \int_{\vec{x}_{snk}} S_\mu(x_{snk},\beta) i\gamma_\sigma S_\mu(\beta,\eta) = \frac{\gamma_0+1}{2} i\gamma_\sigma(-\not{\partial}_y + \gamma_0 + 1)f(\eta-y), \quad (17)$$

$$\lim_{t_{src}\to-\infty} e^{-m_\mu(\eta_t-t_{src})} \int_\alpha G(x,\alpha) \int_{\vec{x}_{src}} S_\mu(\eta,\alpha) i\gamma_\rho S_\mu(\alpha,x_{src}) = (\not{\partial}_x + \gamma_0 + 1) i\gamma_\rho \frac{\gamma_0+1}{2} f(x-\eta), \quad (18)$$

where

$$f(x) = f(|x|, x_t/|x|) = \frac{1}{8\pi^2} \int_0^1 dy\, e^{-yx_t} K_0(y|x|), \quad (19)$$

and $K_0(x)$ is a modified Bessel function of the second kind of order 0. Next, we substitute Eqs. (17) and (18) into Eq. (11) to obtain

$$\mathfrak{G}_{\sigma,\kappa,\rho}(y,z,x) = \frac{\gamma_0+1}{2} i\gamma_\sigma(-\not{\partial}_y + \gamma_0 + 1) i\gamma_\kappa(\not{\partial}_x + \gamma_0 + 1) i\gamma_\rho \frac{\gamma_0+1}{2}$$
$$\times \frac{1}{4\pi^2} \int d^4\eta \frac{1}{(\eta-z)^2} f(\eta-y)f(x-\eta). \quad (20)$$

Before continuing to evaluate this function, let us prove some of its useful properties. It should be noted that based on the definition, Eq. (11), the function $\mathfrak{G}_{\sigma,\kappa,\rho}(y, z, x)$, has a logarithmic infrared divergence. This might raise concern about whether it is correct to evaluate only the QED part of the light-by-light amplitude in infinite-volume. In fact, we show below that the infrared divergence can be avoided by using a new definition of the weighting function.

Recall that γ_μ and $S_\mu(x, y)$ are Hermitian Dirac matrices which satisfy $\Sigma_2 \gamma_\mu \Sigma_2 = (\gamma_\mu)^T$ and $\Sigma_2 S_\mu(x, y) \Sigma_2 = [S_\mu(x, y)]^T$. The free propagator is also translationally invariant, so $S_\mu(x, y) = S_\mu(-y, -x)$. As a result, one can show that

$$\Sigma_2 \mathfrak{G}_{\sigma,\kappa,\rho}(y, z, x) \Sigma_2 = [\mathfrak{G}_{\rho,\kappa,\sigma}(-x, -z, -y)]^T, \quad (21)$$

$$[\mathfrak{G}_{\sigma,\kappa,\rho}(y, z, x)]^\dagger = -\mathfrak{G}_{\rho,\kappa,\sigma}(-x, -z, -y). \quad (22)$$

It immediately follows that

$$\Sigma_2 \mathfrak{G}_{\sigma,\kappa,\rho}(y, z, x) \Sigma_2 = -[\mathfrak{G}_{\sigma,\kappa,\rho}(y, z, x)]^*. \quad (23)$$

Combining this result with Eq. (16), we can parametrize $\mathfrak{G}_{\sigma,\kappa,\rho}(y, z, x)$ as

$$\mathfrak{G}_{\sigma,\kappa,\rho}(y, z, x) = \frac{1 + \gamma_0}{2} [(a_{\sigma,\kappa,\rho}(y, z, x))_k \Sigma_k$$
$$+ i b_{\sigma,\kappa,\rho}(y, z, x)] \frac{1 + \gamma_0}{2}, \quad (24)$$

where $(a_{\sigma,\kappa,\rho}(y, z, x))_k$ and $b_{\sigma,\kappa,\rho}(y, z, x)$ are real functions. Although the function $\mathfrak{G}_{\sigma,\kappa,\rho}(y, z, x)$ is not Hermitian, the non-Hermitian part has no projection to the magnetic

moment. So, for the purpose of obtaining F_2, we only need to evaluate its Hermitian component. Because we need to symmetrize the arguments of the function in Eq. (10), we can freely permute the arguments of $\mathfrak{G}_{\sigma,\kappa,\rho}(y, z, x)$ without changing F_2. This allows us to define a new version of the function:

$$\mathfrak{G}^{(1)}_{\sigma,\kappa,\rho}(y, z, x) = \frac{1}{2} \mathfrak{G}_{\sigma,\kappa,\rho}(y, z, x) + \frac{1}{2} [\mathfrak{G}_{\rho,\kappa,\sigma}(x, z, y)]^\dagger$$
$$= \frac{1}{2} \mathfrak{G}_{\sigma,\kappa,\rho}(y, z, x) - \frac{1}{2} \mathfrak{G}_{\sigma,\kappa,\rho}(-y, -z, -x). \quad (25)$$

As a special case, when all three coordinates are the same, we immediately have

$$\mathfrak{G}^{(1)}_{\sigma,\kappa,\rho}(z, z, z) = 0, \quad (26)$$

since $\mathfrak{G}_{\sigma,\kappa,\rho}(y, z, x)$ only depends on relative coordinates, or the distance between its arguments. Because the divergence of the function $\mathfrak{G}_{\sigma,\kappa,\rho}(y, z, x)$ is infrared and logarithmic, it is independent of the coordinates, x, y, and z. One simple consequence of this behavior and Eq. (26) is that the new version $\mathfrak{G}^{(1)}_{\sigma,\kappa,\rho}(y, z, x)$ is infrared finite. Recall that the new version $\mathfrak{G}^{(1)}_{\sigma,\kappa,\rho}(y, z, x)$ is the same as the original $\mathfrak{G}_{\sigma,\kappa,\rho}(y, z, x)$ after substituting into Eq. (10) and projecting onto the magnetic moment. While the non-Hermitian part of the original QED weighting function has a logarithmic infrared divergence, it does not contribute to the magnetic moment.

With Eqs. (20) and (25), we obtain an infrared finite integration formula for $\mathfrak{G}^{(1)}_{\sigma,\kappa,\rho}(y, z, x)$:

$$\mathfrak{G}^{(1)}_{\sigma,\kappa,\rho}(y, z, x) = \frac{\gamma_0 + 1}{2} i\gamma_\sigma(\partial_\zeta + \gamma_0 + 1) i\gamma_\kappa(\partial_\xi + \gamma_0 + 1) i\gamma_\rho \frac{\gamma_0 + 1}{2}$$
$$\times \frac{1}{4\pi^2} \int d^4\eta \frac{1}{(\eta - z)^2} \frac{f(\eta - y + \zeta)f(x - \eta + \xi) - f(y - \eta + \zeta)f(\eta - x + \xi)}{2} \Bigg|_{\xi=\zeta=0}. \quad (27)$$

This four-dimensional integration is performed with the CUBA library's Cuhre routine [18], which makes use of cubature rules and evaluates the integration in a deterministic way. Since performing the numerical integration is costly and the lattice calculation needs values of this function for many different values of its arguments, we precompute $i^3 \mathcal{G}_{\rho,\sigma,\kappa}(x, y, z)$ for a range of points and then approximate this function by interpolating the computed values, which is similar to the strategy used in Ref. [15]. The arguments of the function $i^3 \mathcal{G}_{\rho,\sigma,\kappa}(x, y, z)$ have 12 degrees of freedom. With the help of translation and spatial rotational symmetries, the relevant number of

degrees of freedom is reduced to five. These five parameters are chosen to be

$$p_0 = (d/6)^{1/2}, \qquad d = |y - z|, \quad (28)$$

$$p_1 = \alpha^{1/2}, \qquad \alpha = |x - z|/d, \quad (29)$$

$$p_2 = \theta/\pi, \qquad \theta = \angle_{y-z,\hat{\imath}}, \quad (30)$$

$$p_3 = \varphi/\pi, \qquad \varphi = \angle_{x-z,\hat{\imath}}, \quad (31)$$

$$p_4 = \eta/\pi, \qquad \eta = \angle_{x-z,y-z}. \quad (32)$$

Because $i^3 \mathcal{G}_{\rho,\sigma,\kappa}(x, y, z)$ is symmetric with respect to permutation of its arguments, without loss of generality, for the purpose of interpolation, we require $|y - z| \geq |x - y| \geq |x - z|$ (this is unrelated to the restriction used for sampling the x-y point pairs on the quark loop). We also limit the length d to be less than 6 (or roughly 11 fm) which should be large enough for the purpose of computing the hadronic light-by-light diagrams on our lattices. We employ a straightforward generalization of bilinear interpolation for the five-dimensional interpolation (the interpolated function is linear with respect to any of its arguments within the small region between the known data points), and the grid has uniform spacing in all directions with $0 \leq p_i \leq 1$. We have computed interpolation grids with sizes 6^5, 8^5, 10^5, 12^5, 14^5, and 16^5. In contrast to Ref. [15], we do not average over the muon propagation direction, so our time direction is special. Thus, we have a five- instead of a three-dimensional grid. The two additional dimensions make the interpolation harder, but, as we shall see, the interpolation error remains under very good control.

Although we introduced $\mathcal{G}^{(1)}_{\sigma,\kappa,\rho}(y, z, x)$ in addition to $\mathcal{G}_{\sigma,\kappa,\rho}(y, z, x)$, their differences will vanish immediately after projecting to the magnetic moment contribution and substituting into Eq. (10). However, due to the conservation of electric current in the hadronic four-point correlation function, we enjoy even more freedom in choosing $\mathcal{G}_{\sigma,\kappa,\rho}(y, z, x)$. We introduce yet another version,

$$\mathcal{G}^{(2)}_{\sigma,\kappa,\rho}(y, z, x) = \mathcal{G}^{(1)}_{\sigma,\kappa,\rho}(y, z, x) - \mathcal{G}^{(1)}_{\sigma,\kappa,\rho}(z, z, x)$$
$$- \mathcal{G}^{(1)}_{\sigma,\kappa,\rho}(y, z, z). \tag{33}$$

With this definition, $\mathcal{G}^{(2)}_{\sigma,\kappa,\rho}(y, z, x)$ has the property that

$$\mathcal{G}^{(2)}_{\sigma,\kappa,\rho}(z, z, x) = \mathcal{G}^{(2)}_{\sigma,\kappa,\rho}(y, z, z) = 0. \tag{34}$$

To demonstrate that these additional two terms in Eq. (33) do not contribute to the final result, recall the current conservation law for $\mathcal{H}^C_{\rho,\sigma,\kappa,\nu}(x, y, z, x_{op})$:

$$\partial_{x_\rho} \left[\sum_{x_{op}} \frac{1}{2} \epsilon_{i,j,k}(x_{op} - x_{ref})_j i \mathcal{H}^C_{\rho,\sigma,\kappa,k}(x, y, z, x_{op}) \right] = 0. \tag{35}$$

Based on arguments similar to those given in Eqs. (22)–(24) of Ref. [11], we conclude that

$$\sum_x \left[\sum_{x_{op}} \frac{1}{2} \epsilon_{i,j,k}(x_{op} - x_{ref})_j i \mathcal{H}^C_{\rho,\sigma,\kappa,k}(x, y, z, x_{op}) \right] = 0, \tag{36}$$

provided surface terms are neglected. Similar conclusions hold for the sums over y and z as well. This implies that

$$\sum_{x,y,z} \mathcal{G}^{(1)}_{\sigma,\kappa,\rho}(y, z, z) \left[\sum_{x_{op}} \frac{1}{2} \epsilon_{i,j,k}(x_{op} - x_{ref})_j i \mathcal{H}^C_{\rho,\sigma,\kappa,k}(x, y, z, x_{op}) \right]$$
$$= 0. \tag{37}$$

This equation demonstrates that if we substitute the subtraction terms defined in Eq. (33) back through Eqs. (10) and (7) and finally into Eq. (4), which gives their contribution to the anomalous moment, we will obtain zero. Since we use Eq. (10) to obtain the QED weighting function, the symmetry between x, y, and z is not affected by the definition of $\mathcal{G}^{(2)}_{\sigma,\kappa,\rho}(y, z, x)$, and Eq. (5) can still be derived for this new function.

The neglect of surface terms in Eqs. (36) and (37) and our use of a nonconserved, local current implies that Eq. (37) strictly holds only in the infinite-volume and continuum limits. In other words, for finite-volume or nonzero lattice spacing, $\mathcal{G}^{(1)}_{\sigma,\kappa,\rho}(y, z, x)$ and $\mathcal{G}^{(2)}_{\sigma,\kappa,\rho}(y, z, x)$ are subject to different finite-volume and lattice spacing effects. Lattice fermion propagators are different from their continuum counterparts mostly in the short-distance region where the source and sink coordinates are the same, or separated by only a few lattice spacings. Hence, the dominant discretization errors most likely come from this region. Since the new QED weighting function satisfies Eq. (34), it will suppress the contribution from this region along with its associated discretization error. As a result, we expect smaller discretization effects if we switch from $\mathcal{G}^{(1)}_{\sigma,\kappa,\rho}(y, z, x)$ to $\mathcal{G}^{(2)}_{\sigma,\kappa,\rho}(y, z, x)$. As we shall see in Sec. III, the new QED weighting function indeed generates a smaller discretization error and, fortunately, a smaller finite-volume error as well.

III. RESULTS

Following Ref. [11], we test this new framework by performing a pure QED light-by-light calculation where the analytic result is well known [19–21]. That is, we replace the quark propagators in Eq. (9) with a leptonic loop. In Ref. [11], we studied the case where the lepton loop mass was equal to the muon mass, $m = m_\mu$. In this study, we also investigate the case where the loop mass is 2 times the muon mass, $m = 2m_\mu$. For both cases, we compare results for weighting functions $\mathcal{G}^{(1)}_{\sigma,\kappa,\rho}(y, z, x)$ and $\mathcal{G}^{(2)}_{\sigma,\kappa,\rho}(y, z, x)$.

We compute F_2 from Eq. (5). As mentioned before, sums over $\tilde{x}_{op}$ and $\tilde{z}$ are performed over the complete lattice volume, but the sum over r is performed stochastically by sampling x-y point pairs. In order to reduce the statistical uncertainty from this stochastic process, we sample all pairs with $r \leq 6$ in lattice units, up to discrete symmetries. These amount to 183 x-y pairs. For $r > 6$, we sample r with the following empirically chosen distribution:

$$p(r) \propto \frac{e^{-2m|r|}}{|r|^3}. \qquad (38)$$

In all the cases presented below, we sampled 4096 pairs with $r > 6$. For each pair, we compute F_2 with the corresponding precomputed, interpolated function $i^3 \mathcal{G}_{\rho,\sigma,\kappa}(x, y, z)$ with grid sizes $N = 6, 8, 10, 12, 14, 16$. The F_2 values for different grids are strongly correlated. We extrapolate to $N \to \infty$ with a second-order fit in $1/N^2$, using three values with $N = 8, 12, 16$. In Fig. 2, we plot fit curves corresponding to typical volumes and lattice spacings for the lepton loop.

After removing the interpolation error for $i^3 \mathcal{G}_{\rho,\sigma,\kappa}(x, y, z)$, we study nonzero lattice spacing and finite-volume effects. The results are plotted in Fig. 3, and the parameter values are listed in Table II. The finite-volume and nonzero lattice spacing effects are greatly reduced by using $\mathcal{G}^{(2)}$ instead of $\mathcal{G}^{(1)}$, and the curves for different volumes appear to be quite parallel. Note that in the latter case some points even have the wrong sign. The difference between the $ma = 0.1$ and $ma = 0.2$ results is a good indicator of the nonzero lattice

spacing effects. Since we have obtained results for $ma = 0.1$ and 0.2 for three volumes, this difference demonstrates the volume dependence of the nonzero lattice spacing effects. We show this comparison in Table III. The $mL = 4.8$ and 6.4 points agree within errors for both loop masses. The volume $mL = 3.2$ shows similar effects, but in some cases, given our high statistical precision, we observe a small difference. This is expected since the nonzero lattice spacing effects become independent of volume in the large volume limit. We also study the lattice spacing dependence of the finite-volume effects in Table IV. It can be seen from the table that the finite-volume effects are roughly independent of lattice spacing. The finite-volume effects at fixed lattice spacing $ma = 0.2$ are shown in Table V, and we expect that the finite-volume effects in the continuum limit are similar. With this table, we can see that the finite-volume effect, falling exponentially with the linear size of the lattice, becomes negligible for $mL = 9.6$.

Since the finite-volume effects are exponentially suppressed with lattice size L and the nonzero lattice spacing effects are of order a^2, the lepton anomaly scales like
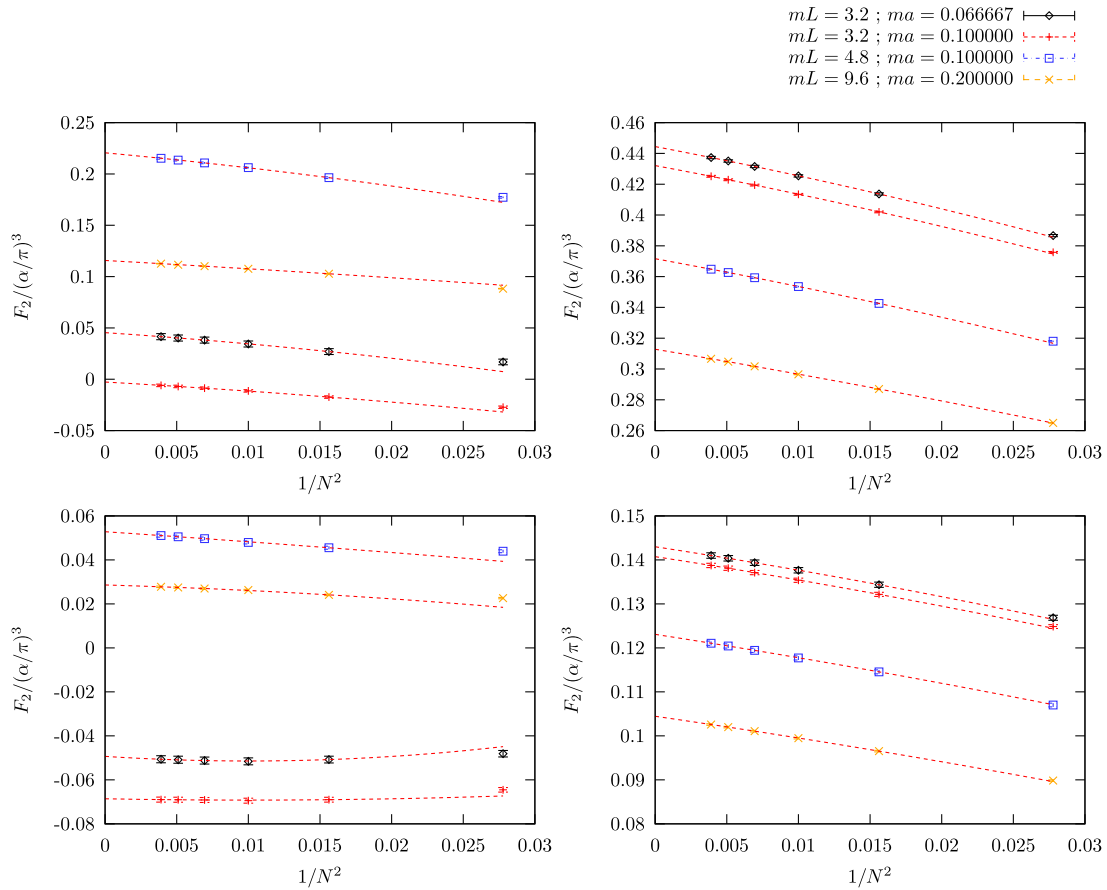

FIG. 2. Extrapolations taking the number of interpolation grid points $N \to \infty$ for various lattices used in this study. The six points for each volume and lattice spacing correspond to $N = 6, 8, 10, 12, 14, 16$. The curves are second-order fits to $1/N^2$, based on the three points $N = 8, 12, 16$. The upper two plots correspond to $m = m_\mu$, the lower two, $m = 2m_\mu$. The left two plots correspond to $\mathcal{G}^{(1)}$, and the right two plots correspond to $\mathcal{G}^{(2)}$.
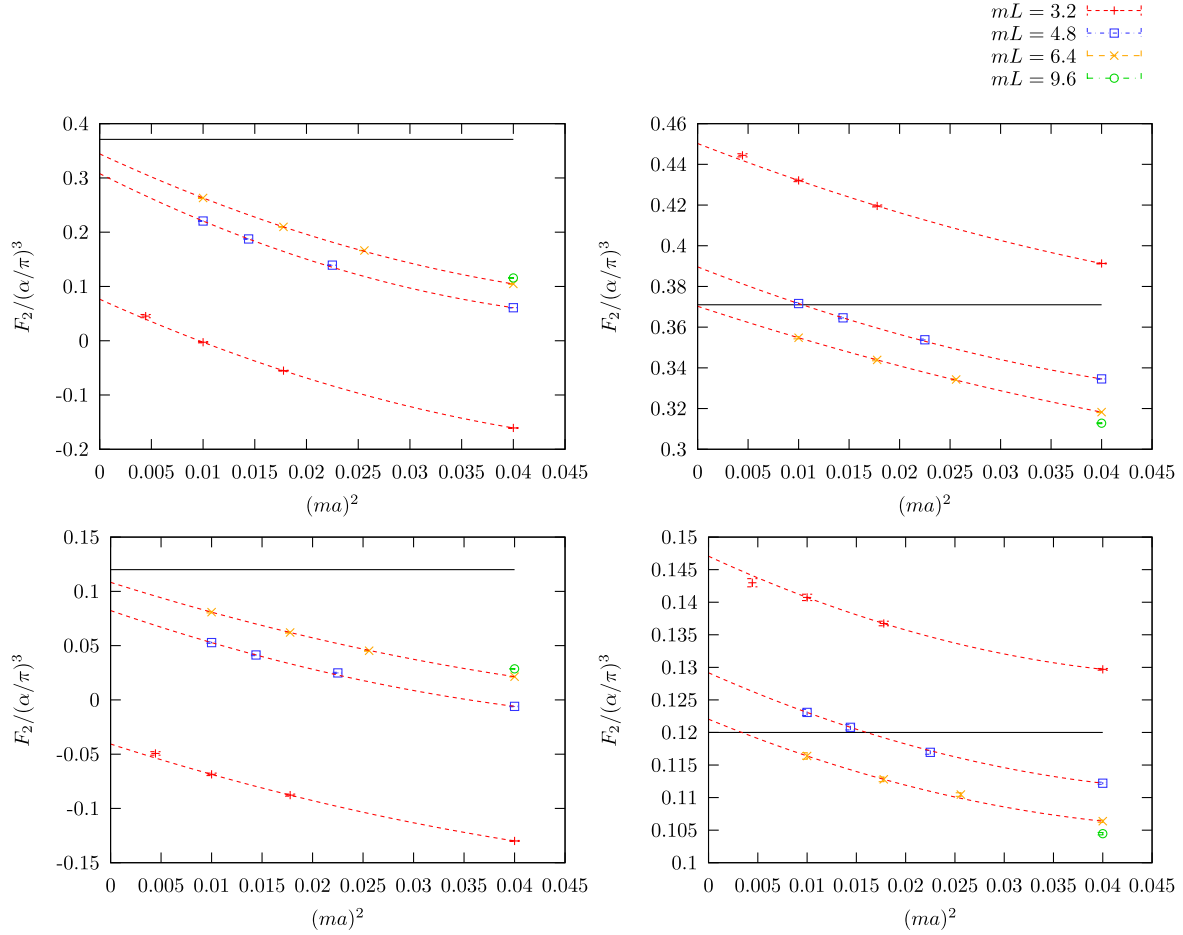
FIG. 3.   Leptonic light-by-light contribution to the muon anomaly, with the lepton loop mass $m = m_\mu$ (upper) and $m = 2m_\mu$ (lower). The continuum, infinite-volume results are $0.371 \times (\alpha/\pi)^3$ for $m = m_\mu$ [19] and $0.120 \times (\alpha/\pi)^3$ for $m = 2m_\mu$ [20,21]. The left two plots correspond to $\mathfrak{G}^{(1)}_{\sigma,\kappa,\rho}(y,z,x)$ and the right two plots to $\mathfrak{G}^{(2)}_{\sigma,\kappa,\rho}(y,z,x)$. For each volume, we draw a second-order line which exactly passes through the three points with $ma = 0.1, 0.12$ or 0.133333, and 0.2 to guide the eye. Note that the vertical scales between the plots on the left and right are different. The discretization error observed on the left is larger than on the right by a factor of 4, or more, while the finite-volume errors are larger by a factor of 2, or more. The parameters for these curves are given in Table II.

$$F_2(L,a) = F_2 + \mathcal{O}(e^{-mL}) + \mathcal{O}((ma)^2). \qquad (39)$$

So far, from Tables III and V, we have made two observations: (1) the nonzero lattice spacing effect becomes approximately independent of volume when $mL \geq 4.8$; (2) the finite-volume effect becomes negligible for

$mL = 9.6$. Based on these two observations, we fit all of the $mL \geq 4.8$ data with the following second-order formula:

$$F_2(L,a) = F_2(L) + k_1 a^2 + k_2 a^4. \qquad (40)$$

TABLE II.   Fits of the muon anomaly after taking the number of interpolation grid points $N \to \infty$ for nonzero lattice spacing shown in Fig. 3.

m/m_μ	mL	$F_2/(\alpha/\pi)^3$ using $\mathfrak{G}^{(1)}$	$F_2/(\alpha/\pi)^3$ using $\mathfrak{G}^{(2)}$
1	3.2	$0.0765(41) - 8.58(37)(ma)^2 + 66(7)(ma)^4$	$0.4502(23) - 1.92(22)(ma)^2 + 11.3(4.1)(ma)^4$
1	4.8	$0.3080(43) - 9.59(44)(ma)^2 + 85(9)(ma)^4$	$0.3896(27) - 1.94(28)(ma)^2 + 14.1(5.3)(ma)^4$
1	6.4	$0.3443(26) - 8.83(23)(ma)^2 + 71(5)(ma)^4$	$0.3703(19) - 1.63(18)(ma)^2 + 8.2(3.4)(ma)^4$
2	3.2	$-0.0407(41) - 2.98(40)(ma)^2 + 19(8)(ma)^4$	$0.1471(18) - 0.70(16)(ma)^2 + 6.6(3.0)(ma)^4$
2	4.8	$0.0823(39) - 3.20(42)(ma)^2 + 25(8)(ma)^4$	$0.1292(26) - 0.67(27)(ma)^2 + 6.2(5.2)(ma)^4$
2	6.4	$0.1083(23) - 2.94(22)(ma)^2 + 19(5)(ma)^4$	$0.1220(17) - 0.62(16)(ma)^2 + 5.8(2.9)(ma)^4$

TABLE III. Volume dependence of nonzero lattice spacing effects in the muon anomaly. Differences between F_2 at $ma = 0.1$ and $ma = 0.2$ are shown for each volume.

m/m_μ	mL	$\Delta F_2/(\alpha/\pi)^3$ using $\mathfrak{G}^{(1)}$	$\Delta F_2/(\alpha/\pi)^3$ using $\mathfrak{G}^{(2)}$
1	3.2	0.1580(13)	0.0408(7)
1	4.8	0.1597(9)	0.0370(6)
1	6.4	0.1584(8)	0.0365(6)
2	3.2	0.0614(13)	0.0110(5)
2	4.8	0.0588(8)	0.0109(5)
2	6.4	0.0594(8)	0.0100(6)

TABLE IV. Lattice spacing dependence of finite-volume effects for the muon anomaly. Differences between F_2 with lattice size L and $6.4/m$ are shown for two lattice spacings, $ma = 0.1$ and $ma = 0.2$.

m/m_μ	mL	ma	$\Delta F_2/(\alpha/\pi)^3$ using $\mathfrak{G}^{(1)}$	$\Delta F_2/(\alpha/\pi)^3$ using $\mathfrak{G}^{(2)}$
1	3.2	0.1	−0.2658(15)	0.0773(9)
1	3.2	0.2	−0.2654(5)	0.0730(4)
1	4.8	0.1	−0.0425(12)	0.0168(8)
1	4.8	0.2	−0.0438(4)	0.0163(4)
2	3.2	0.1	−0.1494(14)	0.0243(7)
2	3.2	0.2	−0.1514(6)	0.0233(3)
2	4.8	0.1	−0.0280(10)	0.0067(7)
2	4.8	0.2	−0.0274(5)	0.0058(3)

To study the systematic effects, we also fit the data with a third-order formula:

$$F_2(L, a) = F_2(L) + k_1 a^2 + k_2 a^4 + k_3 a^6. \tag{41}$$

We do not assume any specific functional form of $F_2(L)$. Instead, we assume

$$F_2 \approx F_2(9.6/m). \tag{42}$$

In this scheme, we show final results for two fermion loop masses and for $\mathfrak{G}^{(1)}$ and $\mathfrak{G}^{(2)}$ in Table VI. We can see that our method, with the third-order fit, has successfully reproduced the analytic calculation within our statistical

TABLE V. Volume dependence of the muon anomaly at fixed nonzero lattice spacing, $ma = 0.2$. It can be seen that the infinite-volume value can be approximated by the largest volume ($mL = 9.6$) result. The column "diff" is the finite-volume effect at this volume and lattice spacing, calculated by taking the difference between $F_2/(\alpha/\pi)^3$ given in that row and in the $mL = 9.6$ row.

m/m_μ	mL	$F_2/(\alpha/\pi)^3$ using $\mathfrak{G}^{(1)}$	Diff	$F_2/(\alpha/\pi)^3$ using $\mathfrak{G}^{(2)}$	Diff
1	3.2	−0.1607(4)	−0.2765(5)	0.3913(3)	0.0785(4)
1	4.8	0.0609(3)	−0.0548(4)	0.3346(3)	0.0217(4)
1	6.4	0.1047(3)	−0.0110(4)	0.3182(3)	0.0054(4)
1	9.6	0.1157(4)	0	0.3128(3)	0
2	3.2	−0.1300(5)	−0.1586(6)	0.1297(2)	0.0252(3)
2	4.8	−0.0060(4)	−0.0346(5)	0.1122(2)	0.0077(3)
2	6.4	0.0214(4)	−0.0072(5)	0.1064(2)	0.0019(3)
2	9.6	0.0286(4)	0	0.1044(2)	0

precision in all cases. For $\mathfrak{G}^{(1)}$, the second-order fits disagree outside of statistical errors, but the values are still quite close, within five percent or less. Using third-order fits and $\mathfrak{G}^{(2)}$ for central values, and the difference between second- and third-order fits as a systematic error, we find

$$F_2/(\alpha/\pi)^3 = 0.3686(37)(35), \tag{43}$$

$$F_2/(\alpha/\pi)^3 = 0.1232(30)(28), \tag{44}$$

for $m/m_\mu = 1$ and 2, respectively. Here, the first error is statistical and the second systematic. These values agree within 1 standard deviation with the analytic results [19–21], 0.371 and 0.120, for the two loop masses.

Finally, to illustrate how exponentially suppressed finite-volume errors compare with the power-law suppressed finite-volume effects seen in Ref. [11], we show the values from Table XI in Ref. [11] and from Table II in Fig. 4. The curves shown in the figure, which are not fits, demonstrate the expected volume dependence of the old finite-volume QED weighting function and the new infinite-volume one. The simple scaling curves also do not account for possible

TABLE VI. The muon anomaly in the continuum and infinite-volume from fits to values with $mL = 4.8, 6.4, 9.6$. Results are given for second-order ($F_2(L) + k_1 a^2 + k_2 a^4$) and third-order ($F_2(L) + k_1 a^2 + k_2 a^4 + k_3 a^6$) fits. Note that "dof" denotes degrees of freedom, and χ^2 is an uncorrelated chi-squared value from the fit. The analytic results are computed using continuum, infinite-volume, perturbation theory [19–21].

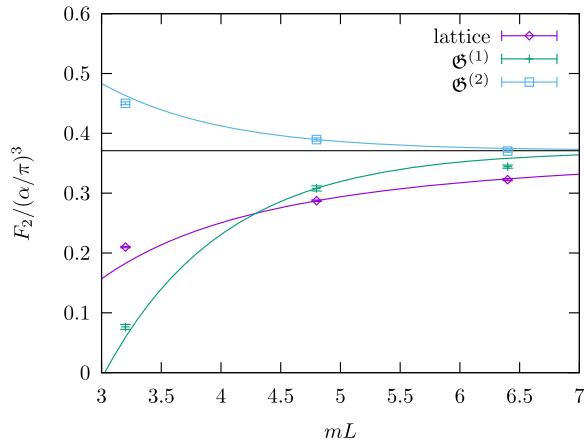| m/m_μ	Order	Dof	$F_2/(\alpha/\pi)^3$ using $\mathfrak{G}^{(1)}$	χ^2	$F_2/(\alpha/\pi)^3$ using $\mathfrak{G}^{(2)}$	χ^2
1	2	$9 - 5 = 4$	0.3522(14)	11.3	0.3651(10)	2.5
1	3	$9 - 6 = 3$	0.3647(51)	2.8	0.3686(37)	1.4
1	Analytic				0.371	
2	2	$9 - 5 = 4$	0.1146(13)	3.6	0.1204(9)	4.5
2	3	$9 - 6 = 3$	0.1153(44)	3.6	0.1232(30)	3.6
2	Analytic				0.120	

FIG. 4. Volume dependence of the muon anomaly for infinite- and finite-volume QED weighting functions. The diamonds correspond to the finite-volume QED weighting function computed on the lattice [11]. The plus signs and squares correspond to infinite-volume QED weighting functions $\mathfrak{G}^{(1)}$ and $\mathfrak{G}^{(2)}$, respectively. Values are listed in Table II. Curves correspond to expected finite-volume scaling $(0.371 + k/L^2)$ and infinite-volume scaling $(0.371 + ke^{-mL})$, where the coefficient k is chosen to match the data at $mL = 4.8$. The rightmost point for the finite-volume weighting function lies a bit off its scaling curve because the discretization error has not been completely removed by the simple ansatz given in Table II, and the coefficient k does not contain any possible volume dependence.

volume dependence of prefactors. The rightmost green, plus sign point for the infinite-volume weighting function $\mathfrak{G}^{(1)}$ lies a bit off the corresponding curve. This most likely results because the discretization error has not been completely removed by the simple ansatz given in Table II. This is confirmed in Table VI, where for $m/m_\mu = 1$ the second- and third-order fit values for $\mathfrak{G}^{(1)}$ do not agree well. Note the second-order fit is especially poor. Still, we can clearly see that the curves for the infinite-volume QED weighting functions approach the analytic result much faster than the curve for the finite-volume QED weighting function, as expected.

IV. CONCLUSION

In this paper we outlined an approach for eliminating the $1/L^2$ finite volume errors in previous hadronic light-by-light calculations [11,13]. This work was very much motivated by the recent progress made in Ref. [15]. In comparison, our approach requires less analytic calculation but more numerical effort. Since we do not average over the direction of the propagating muon line, our function $i^3 \mathcal{G}_{\rho,\sigma,\kappa}(x, y, z)$ depends on five parameters instead of three, which makes the interpolation harder. However, as we have demonstrated in Sec. III, these difficulties have been overcome. We noticed that one has freedom in choosing the QED weighting function $i^3 \mathcal{G}_{\rho,\sigma,\kappa}(x, y, z)$ without affecting the final result. This added freedom can potentially reduce the discretization and finite-volume errors. In particular, we find that the choice $\mathfrak{G}^{(2)}$ defined by Eq. (33) is much better than the original $\mathfrak{G}^{(1)}$ defined in Eqs. (25) and (11). We are now applying the new infinite-volume QED weighting function $i^3 \mathcal{G}_{\rho,\sigma,\kappa}(x, y, z)$ obtained in this work to the hadronic four-point correlation function already computed (and saved) in our previous work [13].

[1] D. Hanneke, S. Fogwell, and G. Gabrielse, New Measurement of the Electron Magnetic Moment and the Fine Structure Constant, Phys. Rev. Lett. **100,** 120801 (2008).

[2] T. Aoyama, M. Hayakawa, T. Kinoshita, and M. Nio, Tenth-order electron anomalous magnetic moment—contribution of diagrams without closed lepton loops, Phys. Rev. D **91,** 033006 (2015).

[3] J. Beringer *et al.*, The review of particle physics, Phys. Rev. D **86,** 010001 (2012).

[4] A. Kurz, T. Liu, P. Marquard, and M. Steinhauser, Hadronic contribution to the muon anomalous magnetic moment to next-to-next-to-leading order, Phys. Lett. B **734,** 144 (2014).

[5] G. W. Bennett *et al.*, Final report of the muon E821 anomalous magnetic moment measurement at BNL, Phys. Rev. D **73,** 072003 (2006).

[6] J. Grange *et al.*, Report Nos. FERMILAB-FN-0992-E, FERMILAB-DESIGN-2014-02, 2015.

[7] M. Davier, A. Hoecker, B. Malaescu, and Z. Zhang, Reevaluation of the hadronic contributions to the muon $(g-2)$ and to $\alpha(M_Z^2)$, Eur. Phys. J. C **71,** 1515 (2011).

[8] K. Hagiwara, R. Liao, A. D. Martin, D. Nomura, and T. Teubner, $(g-2)_\mu$ and $\alpha(M_Z^2)$ re-evaluated using new precise data, J. Phys. G **38,** 085003 (2011).

[9] R. M. Carey *et al.*, Report No. FERMILAB-PROPOSAL-0989, 2009.

[10] M. Aoki *et al.*, An Experimental Proposal on a New Measurement of the Muon Anomalous Magnetic Moment g-2 and Electric Dipole Moment at J-PARC, KEK-J-PARC **PAC2009,** 12 (2009).

[11] T. Blum, N. Christ, M. Hayakawa, T. Izubuchi, L. Jin, C. Jung, and C. Lehner, Lattice calculation of hadronic light-by-light contribution to the muon anomalous magnetic moment, Phys. Rev. D **93,** 014503 (2016).

[12] T. Blum, S. Chowdhury, M. Hayakawa, and T. Izubuchi, Hadronic Light-by-Light Scattering Contribution to the Muon Anomalous Magnetic Moment from Lattice QCD, Phys. Rev. Lett. **114,** 012001 (2015).

[13] T. Blum, N. Christ, M. Hayakawa, T. Izubuchi, L. Jin, C. Jung, and C. Lehner, Connected and Leading Disconnected Hadronic Light-by-Light Contribution to the Muon Anomalous Magnetic Moment with a Physical Pion Mass, Phys. Rev. Lett. **118,** 022005 (2017).

[14] T. Blum, Lattice Calculation of the Lowest Order Hadronic Contribution to the Muon Anomalous Magnetic Moment, Phys. Rev. Lett. **91,** 052001 (2003).

[15] N. Asmussen, J. Green, H. B. Meyer, and A. Nyffeler, Position-space approach to hadronic light-by-light scattering in the muon g—2 on the lattice, Proc. Sci., LATTICE2016 (**2016**) 164 [arXiv:1609.08454].

[16] J. Green, O. Gryniuk, G. von Hippel, H. B. Meyer, and V. Pascalutsa, Lattice QCD Calculation of Hadronic Light-by-Light Scattering, Phys. Rev. Lett. **115,** 222003 (2015).

[17] L. Jin, T. Blum, N. Christ, M. Hayakawa, T. Izubuchi, and C. Lehner, Hadronic light by light contributions to the muon anomalous magnetic moment with physical pions, Proc. Sci., LATTICE2015 (**2016**) 103 [arXiv:1511.05198].

[18] T. Hahn, CUBA: A Library for multidimensional numerical integration, Comput. Phys. Commun. **168,** 78 (2005).

[19] S. Laporta and E. Remiddi, The analytic value of the light-light vertex graph contributions to the electron (g-2) in QED, Phys. Lett. B **265,** 182 (1991).

[20] S. Laporta and E. Remiddi, The analytical value of the electron light-light graphs contribution to the muon (g-2) in QED, Phys. Lett. B **301,** 440 (1993).

[21] J. H. Kuhn, A. I. Onishchenko, A. A. Pivovarov, and O. L. Veretin, Heavy mass expansion, light by light scattering and the anomalous magnetic moment of the muon, Phys. Rev. D **68,** 033018 (2003).

[22] P. A. Boyle, The BAGEL assembler generation library, Comput. Phys. Commun. **180,** 2739 (2009).

[23] M. Frigo, A Fast Fourier Transform Compiler, in *Proceedings of the ACM SIGPLAN 1999 Conference on Programming Language Design and Implementation, USA, 1999*, (ACM, New York, 1999), p. 169.

[24] C. Jung, Overview of Columbia Physics System, Proc. Sci., LATTICE2013 (**2014**) 417.

[25] The CPS software repository can be found at https://github .com/RBC-UKQCD/cps.